Journal of
Applied
Crystallography

ISSN 0021-8898

Received 19 May 2004
Accepted 23 November 2004

© 2005 International Union of Crystallography
Printed in Great Britain – all rights reserved

Analysis of the mosaic structure of an ordered (Al,Ga)N layer

L. Kirste,[a]* K. M. Pavlov,[b] S. T. Mudie,[b] V. I. Punegov[c] and N. Herres[a]‡

[a]Fraunhofer Institut Angewandte Festkörperphysik (FhG-IAF), D-79108 Freiburg, Germany, [b]School of Physics and Materials Engineering, Monash University, Victoria 3800, Australia, and [c]Department of Solid State Physics, Syktyvkar State University, 167001 Syktyvkar, Russia. Correspondence e-mail: lutz.kirste@iaf.fraunhofer.de

The mosaic structure of an (Al,Ga)N layer grown on (0001) sapphire showing natural ordering was studied by high-resolution X-ray diffraction (HRXRD) reciprocal-space mapping. The direction-dependent mosaicity of the layer has been elaborated using maps of symmetrical and asymmetrical reflections. The reciprocal-lattice points show significant broadening depending on the direction in reciprocal space, the diffraction order and the reflection type (fundamental or superstructural). The evaluation followed two paths: (i) a procedure based on the Williamson–Hall plot and (ii) a new approach based on the statistical diffraction theory (SDT). Here, the transformed Takagi equations were implemented for the simulation of the reciprocal-space maps (RSM) for symmetrical and asymmetrical reflections. The reconstruction comprised the mosaic block size, their average rotation angle and the spatial distribution of some components of the microdistortion tensor. The results based on the SDT modelling agree well with those obtained by the Williamson–Hall method, while providing a higher degree of precision and detail.

1. Introduction

(Al,Ga,In) nitrides are important materials for photonic and electronic applications. The physical properties of the epitaxial layers depend on structural features like phase purity, mosaicity, strains and chemical composition. In two earlier papers we addressed problems related to polytypism and texture (Herres *et al.*, 1999) and presented an X-ray diffraction technique suited for the rapid determination of the state of strain and the composition of partially relaxed $Al_xGa_{1-x}N$ and $Ga_{1-x}In_xN$ layers (Herres *et al.*, 2002).

Here, we aim at the evaluation of a layer's defect structure from HRXRD reciprocal-space maps. Crystal defects lead to changes in the width and shape of X-ray diffraction peaks. The amount and orientation of the 'peak broadening' depends on the nature of the crystal defect and will, in general, be different for different reflections (Herres *et al.*, 1996; Ratnikov *et al.*, 2001). Very often the broadening of a 'rocking curve' is used to quantify *e.g.* dislocation densities. However, such rocking curves represent convoluted, projected and experimentally distorted images of the actual situation in reciprocal space and should be looked upon with suspicion unless the nature of the crystal defects present is well known.

Depending on the growth parameters, (Al,Ga,In)N films can show 'natural' ordering of the group-III elements. This chemical ordering is kinetic in nature and a consequence of the large differences of the Al–N, Ga–N and In–N bond strengths. The self-induced ordering is a well known phenomenon in zincblende-type semiconductors (Zunger & Marhajan, 1994). Recently, different types of $Al_xGa_{1-x}N$ wurtzite superstructures have been identified (Korakakis *et al.*, 1997; Iliopoulos *et al.*, 2001; Benamara *et al.*, 2003; Laügt *et al.*, 2003). Ordering is of substantial interest since it is known to influence optical and electronic properties of (Al,Ga,In)-nitride solid solutions (Wright *et al.*, 2001; Dudiy & Zunger, 2003; Albrecht *et al.*, 2004). The formation of a superstructure is indicated by 'superstructure' reflections in diffraction experiments. In general, the formation of a superstructure is not homogeneous throughout the bulk volume and more- and less-ordered regions are commonly observed on a sub-micrometre scale (Follstaedt *et al.*, 1994).

With the present sample, ordered regions do not show the extinction rule for the wurtzite structure; in fact they do not show any *hkl* extinctions at all. In principle, the degree of ordering and the block size of ordered regions is accessible *via* peak heights and peak widths of the X-ray diffraction superstructure reflections.

Numerical fits of scans parallel and perpendicular to the sample surface were performed using Voigt profiles. A procedure similar to a Williamson–Hall plot (Williamson & Hall, 1953; Herres *et al.*, 1996; Balzar, 1999) was applied to obtain direction-dependent crystal sizes, the in-plane strain and the tilt of crystal blocks relative to the surface normal.

‡ Now at: Interstaatliche Hochschule für Technik Buchs NTB, CH-9471 Buchs (SG), Switzerland.

To verify the reconstruction results based on the Williamson–Hall approach, a second evaluation approach used a profile reconstruction technique based on Kato's statistical diffraction theory (SDT) (see *e.g.* Kato, 1980, 1982, 1991, 1994; Bushuev, 1989*a*,*b*; Becker & Haddad, 1990, 1992; Schneider *et al.*, 1992; Takama & Harima, 1994; Guigay & Chukhovskii, 1995; Pavlov & Punegov, 1998, 2000, and references therein). As discussed already by Krivoglaz (1996) the mosaic block model is a rough approximation, and a direct calculation of the appropriate correlation functions of the dislocation deformation field (see *e.g.* Kaganer *et al.*, 1997) is more accurate in most cases. Nevertheless, the mosaic block model is still popular because of its straightforwardness. Different approaches have been used to estimate the parameters of the mosaic block structure from the distribution of the diffracted intensity in the reciprocal space (see *e.g.* Holý *et al.*, 1994; Ratnikov *et al.*, 2001, and references therein). However, these approaches usually give only averaged information about the mosaic block structure, *i.e.* averaged components of the microdistortion tensor.

The approach used in this work allows information about the spatial distribution of the mosaic block parameters to be obtained. For this purpose, the Takagi equations (Takagi, 1969) were transformed to a new form that allows a simulation of the distribution of the diffracted intensity in reciprocal space. The modelling of the mosaic blocks used has been described elsewhere (Nesterets & Punegov, 2000). The parameters used for the reconstruction comprise the size of the blocks, their average rotation angle and spatial distribution of some components of the microdistortion tensor.

2. Experimental

The (Al,Ga)N film investigated here was grown on a (0001) sapphire substrate using plasma-assisted molecular beam epitaxy. Prior to the growth of this film, the substrate was nitridated and a 130 nm AlN buffer layer was deposited at a substrate temperature of 1323 K. The (Al,Ga)N film of 720 nm thickness was deposited at 1093 K.

The lattice parameters of the strained hexagonal metric of the (Al,Ga)N film as determined by extended bond measurements (Herres *et al.*, 2002) were a = 3.1301 and c = 5.0839 Å. After unstraining the unit cell mathematically and interpolating between the lattice parameters of the binary end-members AlN and GaN, the film composition was determined as $Al_{0.56}Ga_{0.44}N$.

During reciprocal-space mapping, the conditioning of the primary X-ray beam [λ(Cu $K\alpha_1$) = 1.54059 Å] was achieved with a parabolically bent graded multilayer mirror and a Bartels–DuMond-type Ge-220 monochromator. For the discrimination of the diffracted X-ray beam, a Bartels–DuMond type Ge-220 analyser was used. Six goniometer axes (Φ, χ, Φ', x, y, z) served to adjust the sample prior to the measurements. Two axes (ω, 2Θ) were positioned and measured under close-loop angular control using incremental optical encoders. The measurement of the diffracted X-ray intensity was performed at equally spaced steps in reciprocal space.

3. Description of the underlying theoretical considerations

A variant of Kato's theory for triple-crystal diffractometry was developed for the dynamical diffraction case (Pavlov & Punegov, 2000) and for the kinematical case (Nesterets & Punegov, 2000). In the present case, the nature of the investigated structure allows us to use a kinematical variant of a new dynamical diffraction approach, a report of which is now in preparation (Pavlov & Punegov, 2005).

We consider the two-beam diffraction in the coplanar Bragg geometry, where the XOY plane is the surface of a crystal, and the XOZ plane is the plane of diffraction. A solution of Maxwell's equations (see *e.g.* Afanas'ev & Kohn, 1971) within the crystal is sought in the following form:

$$\mathbf{E}(\mathbf{r}) = \mathbf{E}_0(\mathbf{r})\exp\left(i\,\mathbf{k}_0^{\rm B}\mathbf{r}\right) + \mathbf{E}_h(\mathbf{r})\exp\left[i\left(\mathbf{k}_0^{\rm B} + \mathbf{h}\right)\mathbf{r}\right]. \qquad (1)$$

Here, following Takagi (1969), we assume that the amplitudes of the transmitted and diffracted waves, $\mathbf{E}_{0,h}(\mathbf{r})$, are slowly varying functions of $\mathbf{r}$. The vector $\mathbf{k}_0^{\rm B}$ can be chosen arbitrarily; in our case this vector is defined as always satisfying the Bragg conditions, with a magnitude of $2\pi/\lambda$, where λ is the X-ray wavelength in vacuum. The vector $\mathbf{h}$ is the appropriate (fixed) vector of the reciprocal lattice. Such definitions allow us to use the coordinates of the point in the reciprocal space directly in the diffraction equations.

Inside the crystal, the X-ray wavefield is described by a system of equations for kinematical diffraction ($\chi_{\bar{h}} \equiv 0$), based on Takagi's equations (Takagi, 1969; Afanas'ev & Kohn, 1971):

$$\begin{aligned}
&\left(\cot\theta_1 \frac{\partial}{\partial x} + \frac{\partial}{\partial z}\right) E_{0,n}(\mathbf{r}) = i a_{0,n} E_{0,n}(\mathbf{r}),\\
&\left(\cot\theta_2 \frac{\partial}{\partial x} - \frac{\partial}{\partial z}\right) E_{h,n}(\mathbf{r}) = i b a_{0,n} E_{h,n}(\mathbf{r})\\
&\qquad\qquad + i a_{h,n} E_{0,n}(\mathbf{r}) \exp[-i\,\mathbf{h}\mathbf{u}(\mathbf{r})],
\end{aligned} \qquad (2a)$$

where

$$a_{0,n}(\mathbf{r}) = \frac{\pi\chi_{0,n}(\mathbf{r})}{\lambda\gamma_0}; \quad a_{h,n}(\mathbf{r}) = \frac{\pi\chi_{h,n}(\mathbf{r})C}{\lambda\gamma_h}; \quad \gamma_{0,h} = \sin\theta_{1,2}.$$

The additional subscript, n, corresponds to the layer number, counted in the direction from the surface toward the substrate. Here, $\chi_{0,h,\bar{h}}$ are the Fourier components of the susceptibility in the layer, C is the polarization factor, $\mathbf{u}(\mathbf{r})$ is the atomic displacement vector (slowly varying function) and $b = \gamma_0/\gamma_h$ is the asymmetry factor. In our definition, $\chi(\mathbf{r}) = s(\mathbf{r})\chi^{\rm ideal}[\mathbf{r} - \mathbf{u}(\mathbf{r})]$, where $\chi^{\rm ideal}(\mathbf{r})$ is the susceptibility of the ideal lattice. The electron density distribution is distorted by two factors: displacement by a vector $\mathbf{u}(\mathbf{r})$, and scaling by $s(\mathbf{r})$, which is responsible for the variation in the chemical composition. Both factors are assumed to be slowly varying functions. The scaling function, $s(\mathbf{r})$, can be represented as a product of two components, $s_{\rm reg}$ and $s_{\rm def}$. The former describes the 'regular' variation of the chemical composition, which has a non-statistical nature. It means that a statistical average of this function, $s_{\rm reg}$, is the function itself. The latter, $s_{\rm def}$, describes the statistical variations of the chemical composition caused by

the structure defects. This function, $s_{\rm def}$, can be presented as a sum of the statistical averaged part, $\langle s_{\rm def}\rangle$, and fluctuation, $\delta s_{\rm def}$. As the function $s_{\rm def}$ is slowly varying, it cannot describe the variation in susceptibility by a segregated point defect. However, this approximation is applicable for defects occupying a few elementary cells, *e.g.* clusters. Therefore, the coefficients in the nth layer in equation (2) can be represented in the form

$$\begin{aligned} a_{i,n}(x,y,z) &= \left[a_{i,n}^{\rm ideal} s_{{\rm reg},n}(x,y)\right] s_{{\rm def},n}(x,y,z) \\ &= a_{i,n}^{\rm reg}(x,y)\, s_{{\rm def},n}(x,y,z) \\ &= a_{i,n}^{\rm reg}(x,y)\left[\left\langle s_{{\rm def},n}(x,y)\right\rangle + \delta s_{{\rm def},n}(x,y,z)\right]. \end{aligned} \quad (2b)$$

where i = 0, h.

The second principal difference from the usual Takagi equations is that we apply equations (2*a*) and (2*b*) for a system of layers, divided by planes parallel to the XOY plane. Within the layer the Fourier components of the susceptibility are slowly varying functions of coordinates X and Y only. This means that the layer thickness in the direction of the Z axis must be small if there is a macroscopic variation of the susceptibility in the Z direction. However, if an analyser crystal and a scintillation detector are employed, as in this article, the dependence on the Y coordinate in equation (2) can be neglected, as this registration system integrates along the Y axis.

The information about deviations of the crystal from the Bragg position is contained in the boundary conditions connecting the wavefield within the crystal [equation (1)] and the wavefield $\mathbf{E}^{\rm v}(\mathbf{r})$ above the crystal surface. The latter can be represented as a combination of the incident and diffracted waves, *i.e.*

$$\mathbf{E}^{\rm v}(\mathbf{r}) = \mathbf{E}_0^{\rm v}(\mathbf{r})\exp(i\mathbf{k}_0^{\rm v}\mathbf{r}) + \mathbf{E}_h^{\rm v}(\mathbf{r})\exp(i\mathbf{k}_h^{\rm v}\mathbf{r}). \quad (3)$$

Here $\mathbf{k}_0^{\rm v}$ is the average wavevector of the incident wave, determined by the monochromator crystals, and $\mathbf{k}_h^{\rm v}$ is the average wavevector selected by an analyser crystal. The total scattering vector is defined as $\mathbf{Q} = \mathbf{k}_h^{\rm v} - \mathbf{k}_0^{\rm v}$ (Iida & Kohra, 1979). Further, we distinguish the components $Q_{x,z}$ from components $q_{hx,0x}$, which are used for the Fourier transform of the wave amplitudes.

Let us perform the following substitution:

$$\begin{aligned} \tilde{E}_{0,n}(x,z) &= E_{0,n}(x,z)\exp\left[ik\omega\gamma_0(x-\cot\theta_1 z)\right] \\ &\quad\times\exp\left\{-i\int\limits_{l_{n-1}}^{z} a_{0,n}\left[x-(z-z')\cot\theta_1\right]{\rm d}z'\right\} \\ &\quad\times\exp\left\{-i\int\limits_{l_{n-2}}^{l_{n-1}} a_{0,n-1}\left[x-(z-z')\cot\theta_1\right]{\rm d}z'\right\} \\ &\quad\ldots\times\exp\left\{-i\int\limits_{0}^{l_1} a_{0,1}\left[x-(z-z')\cot\theta_1\right]{\rm d}z'\right\} \\ &= E_{0,n}(x,z)\exp\left[ik\omega\gamma_0(x-\cot\theta_1 z)\right]/\Omega_{0,n} \end{aligned} \quad (4a)$$

and

$$\begin{aligned} \tilde{E}_{h,n}(x,z) &= E_{h,n}(x,z)\exp\left[ik\gamma_h\omega'(x+\cot\theta_2 z)\right] \\ &\quad\times\exp\left\{ib\int\limits_{l_{n-1}}^{z} a_{0,n}\left[x+(z-z')\cot\theta_2\right]{\rm d}z'\right\} \\ &\quad\times\exp\left\{ib\int\limits_{l_{n-2}}^{l_{n-1}} a_{0,n-1}\left[x+(z-z')\cot\theta_2\right]{\rm d}z'\right\} \\ &\quad\ldots\times\exp\left\{ib\int\limits_{0}^{l_1} a_{0,1}\left[x+(z-z')\cot\theta_2\right]{\rm d}z'\right\} \\ &= E_{h,n}(x,z)\exp\left[ik\gamma_h\omega'(x+\cot\theta_2 z)\right]\Omega_{h,n}. \end{aligned} \quad (4b)$$

Here l_{k-1} is the z coordinate of the top of the kth layer, and ω and ω' are appropriate angular deviations of the vectors $\mathbf{k}_0^{\rm v}$ and $\mathbf{k}_h^{\rm v}$, respectively, from the Bragg conditions for the sample. The new amplitudes $\tilde{E}_{0,h}(x,z)$ are more slowly varying functions than $E_{0,h}(x,z)$ because the exponential terms describing the variations determined by the sample rotation have been separated out. Secondly, the new amplitudes coincide with the wave amplitudes in the vacuum, $E_{0,h}^{\rm v}(x,z)$, at the external surface, where z is equal to 0.

For the sake of simplicity for the final equations, we perform a two-step transformation. Firstly, we will perform the Fourier transform for the amplitudes $\tilde{E}_{0,h}(x,z)$ for the x coordinate to obtain amplitudes $\tilde{E}_0(q_{0x},z)$ and $\tilde{E}_h(q_{hx},z)$ accordingly. Secondly, we replace $\tilde{E}_{0,h}(q_x,z)$ by the new functions $\hat{E}_{0,h}(q_x,z)$, which are still equivalent to the amplitudes $E_{0,h}^{\rm v}(q_x,z)$ at z = 0. These new functions can be represented as follows:

$$\hat{E}_0(q_{0x},z) = \tilde{E}_0(q_{0x},z)\exp(iq_{0x}\cot\theta_1 z) \quad (5a)$$

and

$$\hat{E}_h(q_{hx},z) = \tilde{E}_h(q_{hx},z)\exp(-iq_{hx}\cot\theta_2 z). \quad (5b)$$

The statistical nature of the defects in the samples must still be taken into account. Following the usual procedure described elsewhere (Kato, 1980; Pavlov & Punegov, 2000), we split the wave into the coherent and diffuse parts. The former characterizes the scattering on the average matrix, and the latter originates from scattering by defects. Usually, for the samples investigated, it can be assumed, with good accuracy, that the crystal is homogeneous along the X axis (surface). Also we assume that the incident wave is a plane wave. Then we can write the appropriate equation for the coherent amplitudes:

$$\begin{aligned} &\frac{\partial}{\partial z}\hat{E}_{h,n}^{c}(Q_x,Q_z,q_{hx},z) \\ &\quad= -ia_{h,n}^{\rm reg}\langle s_{{\rm def},n}\rangle\langle\Omega_{0,n}\rangle\langle\Omega_{h,n}\rangle f_n \\ &\qquad\times\exp\Big\{-i\big[Q_z+\Delta q_{z,n}+(Q_x+\Delta q_{x,n})\cot\theta_1 \\ &\qquad+q_{hx}(\cot\theta_1+\cot\theta_2)\big]z\Big\}\delta(Q_x+q_{hx}+\Delta q_{x,n}), \end{aligned} \quad (6)$$

where $\delta(q)$ is a delta function, $\Delta q_{x,n}$ and $\Delta q_{z,n}$ are appropriate shifts due to the averaged homogeneous deformation for the nth layer, namely $\mathbf{hu}_{\rm hom} = \Delta q_x x + \Delta q_z z$, f_n is the static Debye–Waller factor for the nth layer, and terms $\Omega_{0,h}$, describing the attenuation effects, are defined in equation (4), similar to $\Phi_{0,h}$ as given by Nesterets & Punegov (2000). We explicitly show in

equation (6) and in the rest of the article that the amplitude of the diffracted wave depends on the vector **Q**.

The following are the equations for the diffuse intensities:

$$\begin{aligned}\partial\hat{I}^{\rm d}_{h,n}(Q_x, Q_z, q_{hx}, z)/\partial z \\ = -|a^{\rm reg}_{h,n}|^2\langle s_{{\rm def},n}\rangle^2(1-f_n^2)\hat{\tau}^*_{1,n}(Q_x, Q_z, q_{hx}, 0) \\ - |a^{\rm reg}_{h,n}|^2 f_n^2\Big(1-\langle s_{{\rm def},n}\rangle^2\Big)\hat{\tau}^*_{3,n}(Q_x, Q_z, q_{hx}, 0) + {\rm c.c.}\end{aligned} \quad (7)$$

where the differential correlation areas are given in the form [*cf.* equation (18) of Pavlov & Punegov (2000)]

$$\begin{aligned}\hat{\tau}_{1,n}(Q_x, Q_z, q_x, \tilde{q}_x) \\ = [1/(1-f_n^2)]\int\limits_0^{l_n - z\simeq\infty}{\rm d}\xi\int{\rm d}\varepsilon \\ \times \exp[-i(Q_z + \Delta q_{z,n} + q_x\cot\theta_2 + \tilde{q}_x\cot\theta_1)\xi] \\ \times \exp[-i(Q_x + \Delta q_{x,n} + q_x - \tilde{q}_x)\varepsilon] \\ \times \langle\delta\Phi^*(\varepsilon,\xi)\delta\Phi(0,0)\rangle \\ \times \langle\Omega_{0,n}(\varepsilon, l_{n-1}+\xi)\rangle\langle\Omega_{h,n}(\varepsilon, l_{n-1}+\xi)\rangle \\ \times [\langle\Omega^*_{0,n}(0, l_{n-1})\rangle\langle\Omega^*_{h,n}(0, l_{n-1})\rangle]\end{aligned} \quad (8a)$$

and

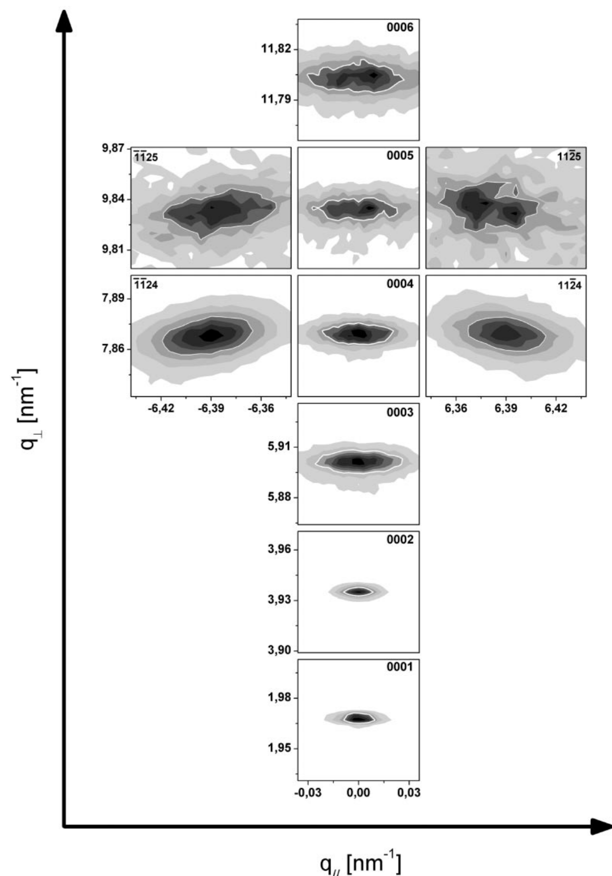

Figure 1
Reciprocal-space maps of the ordered $Al_{0.56}Ga_{0.44}N$ layer.

$$\begin{aligned}\hat{\tau}_{3,n}(Q_x, Q_z, q_x, \tilde{q}_x) \\ = \Big[1/\Big(1-\langle s_{{\rm def},n}\rangle^2\Big)\Big]\int\limits_0^{l_n - z\simeq\infty}{\rm d}\xi\int{\rm d}\varepsilon \\ \times \exp[-i(Q_z + \Delta q_{z,n} + q_x\cot\theta_2 + \tilde{q}_x\cot\theta_1)\xi] \\ \times \exp[-i(Q_x + \Delta q_{x,n} + q_x - \tilde{q}_x)\varepsilon] \\ \times \langle\delta s_{{\rm def},n}(\varepsilon,\xi)\delta s_{{\rm def},n}(0,0)\rangle \\ \times \langle\Omega_{0,n}(\varepsilon, l_{n-1}+\xi)\rangle\langle\Omega_{h,n}(\varepsilon, l_{n-1}+\xi)\rangle \\ \times [\langle\Omega^*_{0,n}(0, l_{n-1})\rangle\langle\Omega^*_{h,n}(0, l_{n-1})\rangle].\end{aligned} \quad (8b)$$

For the X-ray diffraction simulations in this paper, we can neglect the second term ($\sim f_n^2$) in equation (7) because of the low value of the static Debye–Waller factor f_n.

The total intensity registered by the detector is

$$\begin{aligned}I^{\rm det}(Q_x, Q_z) = \int{\rm d}q_{hx}\,R(q_{hx})\big|E^{\rm v}_h(Q_x, Q_z, q_{hx}, 0)\big|^2 \\ \equiv \int{\rm d}q_x\,R(q_{hx})\Big[\Big|\hat{E}^{\rm c}_{h,1}(Q_x, Q_z, q_{hx}, 0)\Big|^2 \\ + \hat{I}^{\rm d}_{h,1}(Q_x, Q_z, q_{hx}, 0)\Big],\end{aligned} \quad (9)$$

where $R(q_{hx})$ is the reflectivity of the analyser crystals.

The mosaic blocks are considered to be brick shaped with dimensions L_x and L_z along the appropriate axes. The rotation of the mosaic blocks around the Y axis is described by a Gaussian function. The correlation function $\langle\delta\Phi^*(\varepsilon,\xi)\,\delta\Phi(0,0)\rangle$ for the model of mosaic blocks, used in our simulation, is described elsewhere (Nesterets & Punegov, 2000).

4. Results and discussion

4.1. Observation and profile fit of the broadened diffraction peaks

The present $Al_{0.56}Ga_{0.44}N$ layer showed chemical ordering where the metal ions preferentially occupy lattice sites in such a way that alternating Al and Ga layers are stacked along the [0001] growth direction. This phenomenon can be traced by measuring the 'superstructure' peaks with the scattering conditions $h + 2k = 3n$ and l = odd, and can be clearly separated from the commonly observed polytypism in (Al,Ga,In)N layers. The metal-ion space-group symmetry is reduced from $P6_3mc$ of the wurtzite structure type to $P3m1$.

In order to examine the defect structure of the $Al_{0.56}Ga_{0.44}N$ layer, reciprocal-space maps (RSMs) of the fundamental peaks (0002, 0004, 0006, $\bar{1}\bar{1}24$ and $11\bar{2}4$) and superstructure peaks (0001, 0003, 0005, $\bar{1}\bar{1}25$ and $11\bar{2}5$) were measured (Fig. 1). The reciprocal-lattice points show a significant amount of broadening depending on the direction in reciprocal space, diffraction order and reflection type (fundamental or superstructure reflection), indicating the mosaicity of the layer. For a more detailed consideration of the peak broadening, we performed additional reciprocal-space scans (RSS) with higher resolution through the intensity maxima parallel to the $q_\perp$ and the $q_\parallel$ direction (Figs. 2*a* and 2*b*).

Table 1
Experimentally observed peak positions and peak broadenings of superstructure ('odd') and fundamental ('even') 000l reflections.

	Peak position		Peak broadening (Voigt profiles)				
Reflection $hkil$	$q_\perp$ (nm^{-1})	2Θ (°)	$\Delta q_{\|}$ (nm^{-1})	$\Delta\omega$ (°)	$\Delta q_\perp$ (nm^{-1})	$\Delta 2\Theta$ (°)	Intensity (c.p.s.)
0001	1.967	17.427	0.0163	0.475	0.0032	0.029	33.72
0002	3.933	35.274	0.0193	0.281	0.0055	0.051	294.60
0003	5.900	54.062	0.0336	0.326	0.0084	0.083	1.54
0004	7.867	74.597	0.0348	0.254	0.0107	0.118	8.93
0005	9.833	98.481	0.0474	0.276	0.0136	0.184	0.23
0006	11.800	130.721	0.0497	0.241	0.0163	0.345	1.79

4.2. Peak broadening analysis using a Williamson–Hall procedure

In order to extract structural information from the peak broadenings, a technique similar to the Williamson–Hall evaluation procedure was used (Williamson & Hall, 1953; Herres *et al.*, 1996; Balzar, 1999). Here, for a series of reflections, the direction-dependent broadening of each peak is plotted *versus* its location in reciprocal space. The slope and intercept of the best-fit straight lines then serve to deduce two sets of structural parameters. (i) Using the broadenings, $\Delta q_\perp$, of reciprocal-lattice peaks perpendicular to the film's surface, the average size of crystallites in this direction is obtained from the intercept, and the average inhomogeneous strain in this direction is obtained from the slope. (ii) Using the broadenings, $\Delta q_{\|}$, of reciprocal-lattice peaks parallel to the film's surface, the average size of crystallites in this direction is obtained from the intercept, and the average tilt of the crystallites relative to the film's surface is obtained from the slope.

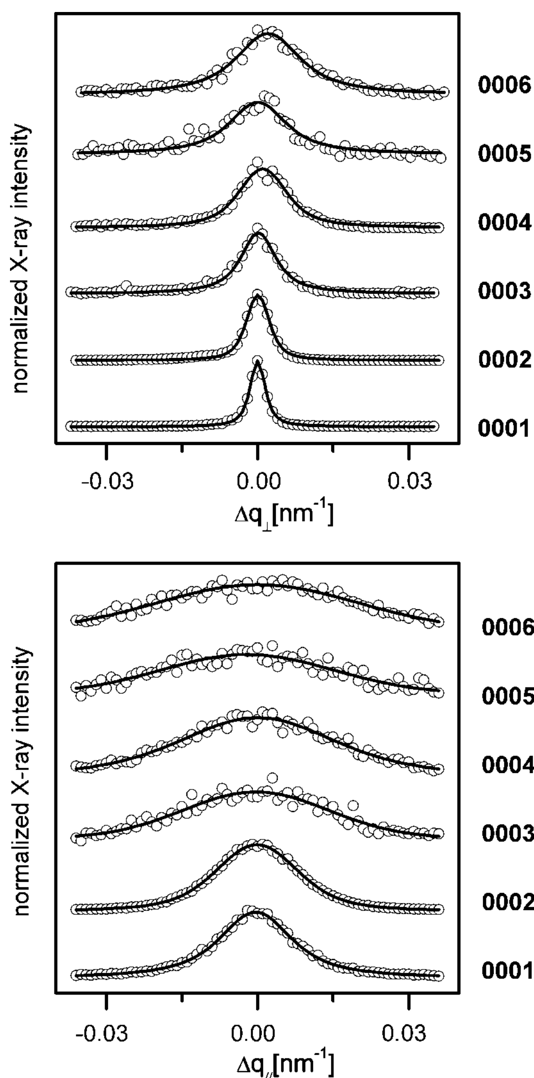

Figure 2
Reciprocal-space scans taken perpendicular and parallel to the growth surface of the ordered $Al_{0.56}Ga_{0.44}N$ layer. The scans have been fitted using Voigt profiles.

In the presence of Lorentz peak profiles, the Williamson–Hall procedure uses linear regression in Δq–q space. With Gaussian peak profiles, the linear regression is performed in Δq^2–q^2 space. In practice, very often, neither pure Gaussian nor pure Lorentzian profiles are observed. In the present case, only Voigt profiles (a combination of a Gaussian and a Lorentzian distribution) allowed a nearly perfect fit of all peaks profiles (Figs. 2*a* and 2*b*). The integral breadth β of the Voigt function was calculated from its Gaussian and Lorentzian components using the relationship $\beta^2 = \beta_{\rm Lorentz}\beta + \beta^2_{\rm Gauss}$ (Halder & Wagner, 1966). The numerical values thus obtained are the 'reflection broadening' $\Delta\omega = \beta$ for the subsequent evaluations. Table 1 summarizes the input data for the Williamson–Hall evaluation.

Fig. 3 shows two Williamson–Hall plots for the symmetrical 000l reflections drawn in Δq^2–q^2 space. Fig. 3(*a*) is drawn using the peak broadenings $\Delta q_\perp$ perpendicular to the sample surface, whereas in Fig. 3(*b*) the peak broadenings $\Delta q_{\|}$ parallel to the sample surface were used. Surprisingly, good fits were obtained with linear regressions in both kinds of Williamson–Hall plots: in Δq^2–q^2 space and in Δq–q space. However, the resulting structural parameters (direction-dependent crystal sizes, tilt relative to the surface normal and strain) significantly differ, as shown in Table 2. Thus, the use of the integral breadth of the Voigt function (composed of a Gaussian and a Lorentzian function) in such Williamson–Hall plots is problematic and may only be cautiously interpreted.

The evaluation of the data shows that the crystalline size $L_\perp$ perpendicular to the surface of the layer, which is the size of the coherently reflecting domains as obtained from the intercept of the ordinate, is 709 ± 363 nm for the analysis in Δq^2–q^2 space and 2315 ± 692 nm for the analysis in Δq–q space. The value of 709 nm for $L_\perp$ is corroborated by a Rutherford

Table 2
Parameters describing the film's mosaicity as obtained by the Williamson–Hall procedure.

(*a*) Results from linear regression within a Δq^2–q^2 plot.

	$L_{\parallel}$ (nm)	τ (°)	$L_{\perp}$ (nm)	$\langle\varepsilon_{zz}\rangle$ ($\times10^{-3}$)
Using fundamental ('even') reflections	88 ± 31	0.24 ± 0.04	709 ± 363	2.75 ± 0.34
Using superlattice ('odd') reflections	61 ± 26	0.26 ± 0.09		

(*b*) Results from linear regression within a Δq–q plot.

	$L_{\parallel}$ (nm)	τ (°)	$L_{\perp}$ (nm)	$\langle\varepsilon_{zz}\rangle$ ($\times10^{-3}$)
Using fundamental ('even') reflections	237 ± 23	0.22 ± 0.01	2315 ± 692	2.66 ± 0.05
Using superlattice ('odd') reflections	102 ± 13	0.22 ± 0.01		

backscattering measurement, which yielded a layer thickness of 720 nm.

The analysis of the peaks in the $\Delta q_{\parallel}$ direction (Δq^2–q^2 space) shows that there is a different amount of broadening for the superstructure and the fundamental reflections, which were thus treated separately. The mosaicity tilt τ with respect to the surface normal amounts to roughly 0.25 ± 0.05° for both fundamental and superstructure reflections. However, the crystalline size $L_{\parallel}$ parallel to the surface of the layer yields a value of 88 ± 31 nm when deduced from fundamental reflections, but only 61 ± 26 nm when deduced from superstructure reflections. This discrepancy in crystal size $L_{\parallel}$ can be explained by the formation of chemical antiphase domain boundaries (APDs) with boundaries disturbing the group-III element modulation. A model of these APDs is shown in Fig. 8. The formation of APDs is a well known phenomenon in zincblende-type semiconductors, *e.g.* (In,Ga)P, showing ordering (Bellon *et al.*, 1989; Follstaedt *et al.*, 1994). In Appendix *A* (case 1) we discuss how antiphase domains lead to the pronounced additional broadening of the 000*l* superstructure reflections and why there is no such additional broadening in the fundamental reflections.

Korakakis *et al.* (1997) also observed in θ–2θ scans a different broadening for the symmetrical fundamental and superstructure reflections for an (Al,Ga)N layer. They state that this broadening 'can be attributed to either size effect broadening or formation of antiphase domains'. However, as detailed in Appendix *A*, antiphase domains will lead to a broadening of 000*l* reflections parallel to the $q_{\parallel}$ direction only for superstructure reflections (case 1), whereas no broadening will be observable parallel to the $q_{\perp}$ direction (case 2). Our experimental results support this theory, showing the difference in broadening between fundamental and superstructure reflections only in the $q_{\parallel}$ direction.

An explanation for the observation of Korakakis *et al.* (1997) may be that they did not use a proper analyser crystal,

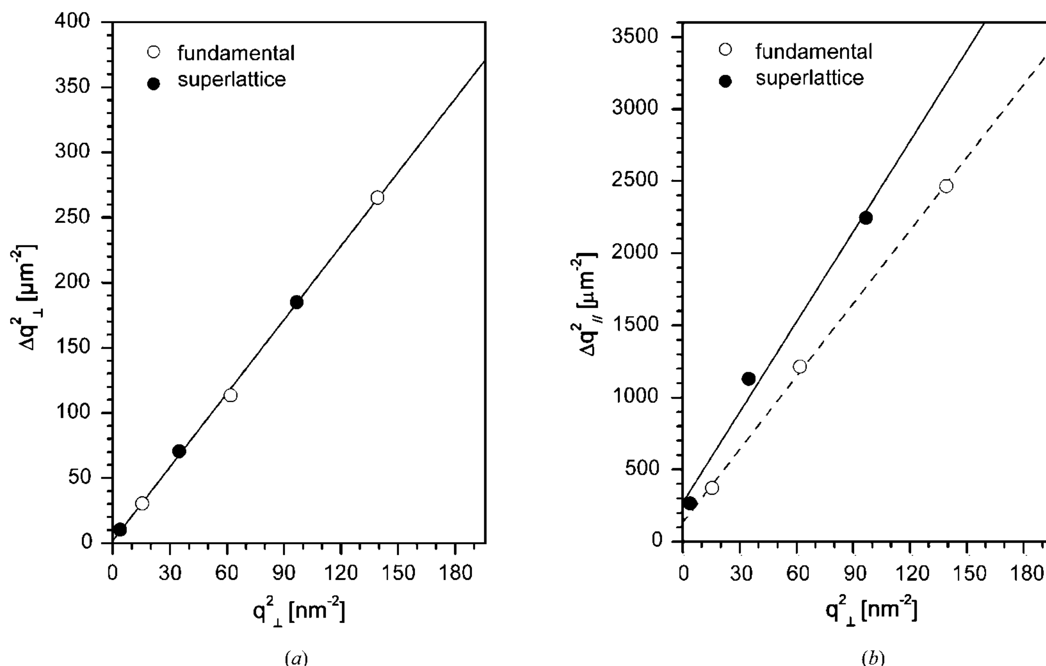

Figure 3
Williamson–Hall plots of the 000*l* reflections in Δq^2–q^2 space. Plot (*b*), based on peak widths $\Delta q_{\parallel}$ parallel to the growth surface, shows different regression lines for the fundamental peaks and the peaks due to ordering.

Table 3
Parameters describing the film's mosaicity as obtained by peak profile modelling based on the SDT.

	$L_{\parallel 1}$ (nm)	$L_{\parallel 2}$ (nm)	τ (°)	$L_{\perp}$ (nm)	$\langle \varepsilon_{xx} \rangle$ ($\times 10^{-3}$)	$\langle \varepsilon_{zz} \rangle$ ($\times 10^{-3}$)
Using fundamental ('even') reflections	90 ± 10	n.a.	0.29 ± 0.03	740	11	2.7
using superlattice ('odd') reflections	65 ± 7	24 ± 3	0.30 ± 0.03			

thus broadening the probe in reciprocal space along a line oblique to the $q_{\perp}$ direction. Hence the recorded peak is a convolution of this probe and the diffraction spot (in reciprocal space). In this case the observed peak shape and width depends on the nature of the sample in both the $q_{\perp}$ and $q_{\parallel}$ directions, and is hence sensitive to the lateral antiphase domain structure. We have negated this effect for our experiments by using a Bartels–DuMond analyser setup, which reduces the size of the probe in reciprocal space dramatically.

In order to obtain a rough estimate of the long-range order parameter S (see Appendix A) the observed peak intensities for the 0001 and 0004 reflections were modelled. The value obtained, $S \simeq 0.2$, is most likely too low because we did not properly account for surface roughness.

4.3. Peak broadening analysis using the statistical diffraction theory approach

The statistical diffraction theory and mosaic block model described in §3 were used to simulate scans in both the $q_{\perp}$ and $q_{\parallel}$ directions. The model parameters used for fitting were the sizes of the mosaic blocks, the spread of the mosaicity tilt angle and the distribution of microdistortion components $\varepsilon_{xx}(z)$ and $\varepsilon_{zz}(z)$. For the scans in the $q_{\parallel}$ direction, the parameters effected the simulation were the lateral size of the mosaic blocks, $L_{\parallel}$, the spread of the mosaicity tilt angle and the distribution of microdistortion components $\varepsilon_{xx}(z)$. The $q_{\perp}$ scans furnished information about the strain distribution $\varepsilon_{zz}(z)$ and the mosaic block size, $L_{\perp}$, perpendicular to the surface.

For the $q_{\parallel}$ scans it was necessary to analyse odd reflections (0001, 0003, 0005) and even reflections (0002, 0004, 0006) separately, because of the antiphase domain structure. For an even reflection there is no phase shift at antiphase domain boundaries (as given by the structure factor); however, for an odd reflection there will be a phase shift. Figs. 4 and 5 show fitted data for the 0001 and 0002 scans, respectively. The dependence of the simulated curve on the various fitting parameters is indicated in both figures by the dotted (increased 10%) and dashed (decreased 10%) curves. The material's parameters are summarized in Table 3.

The experimental data for the odd reflections could not be fitted accurately using only one block size and tilt distribution width due to the different line shape. Hence the model was extended to allow two lateral block sizes to exist simultaneously. This modified the shape of the simulated scan, and with optimized parameters allowed it to be matched to the data as shown in Fig. 4. Agreement was seen for the tilt spread determined from both reflection types. This was encouraging as topologically they should be the same value.

In order to fit the $q_{\perp}$ scans for symmetrical reflections and $q_{\parallel}$ scans for asymmetrical reflections, 60 sublayers were required to simulate the strain distribution $\varepsilon_{xx}(z)$ and $\varepsilon_{zz}(z)$. The variation of strain is shown in Fig. 6. Note that this strain is asymmetric about zero. Fig. 7 shows fitted data for the $q_{\parallel}$

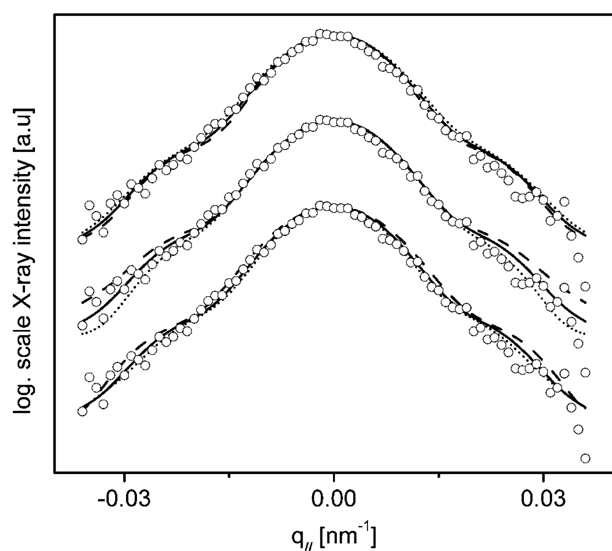

Figure 4
Experimental data (circles) and simulations (lines) for the $q_{\parallel}$ scan through the 0001 reflection (logarithmic intensity scale). The top curve shows the effect of varying τ, the middle curve that of varying $L_{\parallel 2}$ and the bottom curve that of varying $L_{\parallel 1}$. (Dotted +10%, dashed −10% of appropriate parameters.)

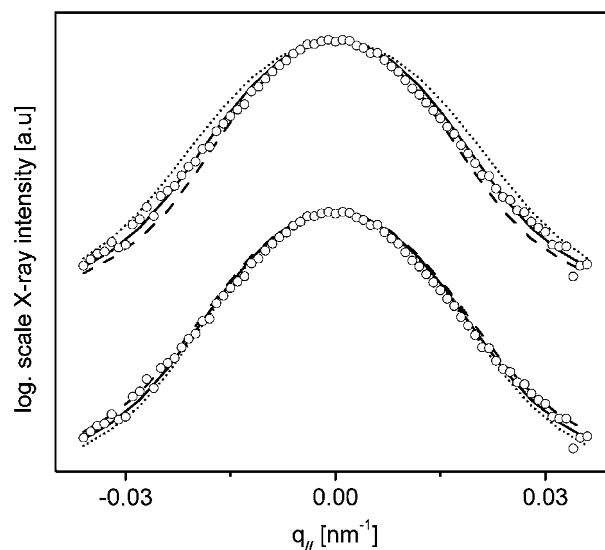

Figure 5
Experimental data (circles) and simulations (lines) for the $q_{\parallel}$ scan through the 0002 reflection (logarithmic intensity scale). The top curve shows the effect of varying τ and the bottom that of varying $L_{\parallel}$. (Dotted +10%, dashed −10% of appropriate parameters.)

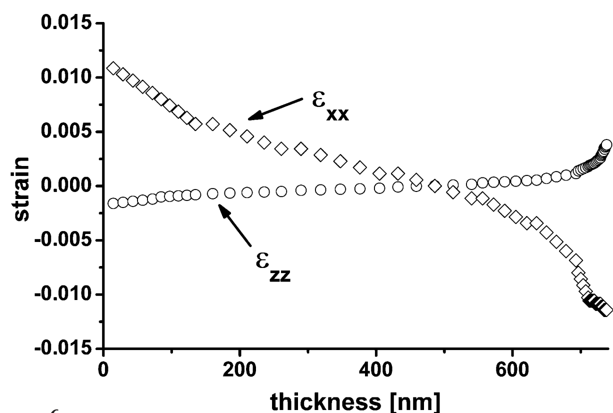

Figure 6
The variation in the strain components.

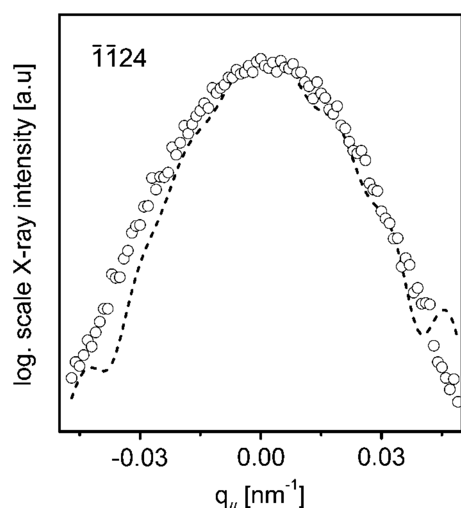

Figure 7
Experimental data (circles) and simulations (dashed line) for a $q_{\|}$ scan through the $\bar{1}\bar{1}24$ reflection.

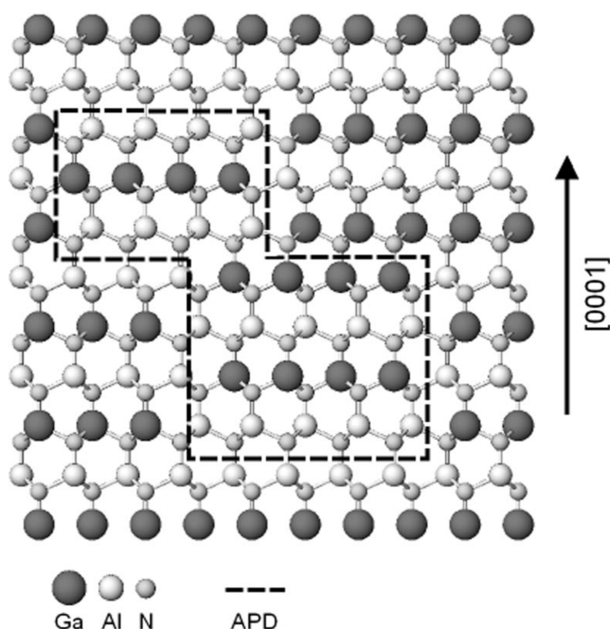

Figure 8
Model of chemical antiphase domain boundaries in ordered $Al_{0.5}Ga_{0.5}N$ layers.

scan about $\bar{1}\bar{1}24$. Asymmetric reflections were used to reconstruct the distribution of the strain component $\varepsilon_{xx}(z)$, which is larger than $\varepsilon_{zz}(z)$. The reason for this might be the presence of threading dislocations, which lie parallel to [0001] direction and are pure edge with Burgers vectors parallel to the surface (Heying *et al.*, 1996). All simulated RSMs are presented in Fig. 9.

5. Conclusions

A high level of agreement was seen between the results determined by simulation and the traditional Williamson–Hall analysis. Specifically, both the tilt and thickness values agree within their uncertainty ranges. Furthermore, a comparison of the simulated block sizes (using the larger value for the odd reflections), agrees with the data determined from linear regression within Δq^2–q^2 space for the Williamson–Hall analysis, but not within Δq–q space. Finally, the average strain $\langle\varepsilon_{zz}\rangle$ obtained by the SDT agrees with the Williamson–Hall analysis. At present, the ease of use still speaks for the Williamson–Hall method; however, its limitations become more and more obvious with complex defect structures.

The reconstruction method based on SDT offers a number of improvements over the traditional fitting regime. Firstly, this method can handle more complex systems (*e.g.* various block sizes, sublayers, strain gradients, *etc*). This is impossible with traditional analysis techniques like the Williamson–Hall plot, where in principle just two structural parameters can be

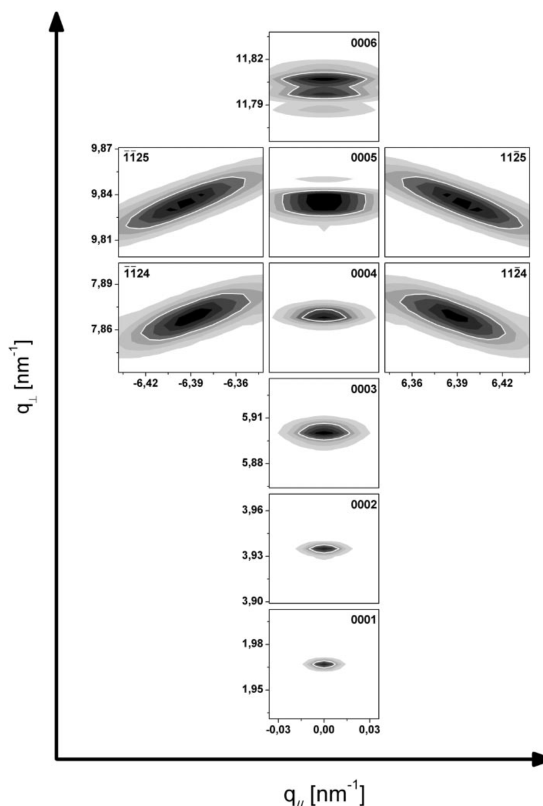

Figure 9
The simulated reciprocal-space maps (to be compared with Fig. 1).

deduced from each plot. Secondly, by using real structural parameters to simulate intensity profiles we can remove the restriction that the curve be of a particular shape, thus allowing the fine structure of the experimental curve to be used in the fitting procedure. We can therefore expect the simulations based on SDT to produce more reasonable data than Williamson–Hall evaluations, in particular with complex defect structures.

APPENDIX *A*
Long-range ordering and antiphase domains

Here we discuss two issues, namely, long-range ordering and antiphase domains (see *e.g.* Warren, 1969), which we employed in order to elucidate the experimental data.

The structure factor of the (Al,Ga)N 'naturally' ordered structure can be written as:

$$\begin{aligned}F_{hkl} = {} & \left(r_1 f_{\rm Ga} + w_1 f_{\rm Al}\right) \exp\left[-2\pi i\left(\tfrac{1}{3}h + \tfrac{2}{3}k\right)\right] \\ & + \left(r_2 f_{\rm Al} + w_2 f_{\rm Ga}\right) \exp\left[-2\pi i\left(\tfrac{2}{3}h + \tfrac{1}{3}k + \tfrac{1}{2}l\right)\right] \\ & + f_N \exp\left[-2\pi i\left(\tfrac{1}{3}h + \tfrac{2}{3}k + \tfrac{3}{8}l\right)\right] \\ & + f_N \exp\left[-2\pi i\left(\tfrac{2}{3}h + \tfrac{1}{3}k + \tfrac{7}{8}l\right)\right]. \end{aligned} \qquad (10)$$

Here r_1 = fraction of atom1 sites occupied by the 'right' atom (Ga), r_2 = fraction of atom2 sites occupied by the 'right' atom (Al), w_1 = fraction of atom1 sites occupied by the 'wrong' atom (Al), w_2 = fraction of atom2 sites occupied by the 'wrong' atom (Ga).

Several relations between the parameters are obvious:

$$r_1 + w_1 = 1, \quad r_2 + w_2 = 1, \quad r_1 + w_1 = r_2 + w_2.$$

The composition of the sample is represented by the atom fractions $n_{\rm Al}$ and $n_{\rm Ga}$, where $n_{\rm Al} + n_{\rm Ga} = 1$. In a stoichiometric sample, the following relations are applicable:

$$n_{\rm Al} = \tfrac{1}{2}(r_2 + w_1), \quad n_{\rm Ga} = \tfrac{1}{2}(r_1 + w_2).$$

Following Warren (1969), we introduce a long-range order parameter S in the following form:

$$S = r_1 + r_2 - 1 = r_1 - w_2 = r_2 - w_1 = 2\left(r_1 - n_{\rm Ga}\right). \qquad (11)$$

This parameter S reaches its maximum value of unity only for the stoichiometric composition ($n_{\rm Al} = n_{\rm Ga} = 0.5$); for a nonstoichiometric composition the parameter value will always be less than unity. In the present case, $n_{\rm Al} = 0.564$ and thus $n_{\rm Ga} = 0.436$ (as shown by lattice-parameter measurements). However, the observed deviation from stoichiometry is of minor importance because the structure factors for the superstructure reflections are proportional to S even for nonstoichiometric compositions.

From equation (10), the structure factors for the 'fundamental' reflections (0002, 0004, 0006) are

$$\begin{aligned}F_{hkl} & = \left(r_1 f_{\rm Ga} + w_1 f_{\rm Al}\right) + \left(r_2 f_{\rm Al} + w_2 f_{\rm Ga}\right) + 2 f_{\rm N} \exp\left[-2\pi i\left(\tfrac{3}{8}l\right)\right] \\ & = 2 n_{\rm Ga} f_{\rm Ga} + 2 n_{\rm Al} f_{\rm Al} + 2 f_{\rm N} \exp\left[-2\pi i\left(\tfrac{3}{8}l\right)\right], \end{aligned} \qquad (12)$$

where l = 2, 4, 6.

For the 'superstructure' reflections (0001, 0003, 0005), the structure factors can be rewritten as

$$F_{hkl} = \left(r_1 f_{\rm Ga} + w_1 f_{\rm Al}\right) - \left(r_2 f_{\rm Al} + w_2 f_{\rm Ga}\right) = S\left(f_{\rm Ga} - f_{\rm Al}\right). \qquad (13)$$

The structure factor of the 'superstructure' reflections [equation (13)] directly depends of the long-range order parameter S, unlike the structure factor for the 'fundamental' reflections [equation (12)]. The parameter S can be determined during the simulations of the diffracted intensity [equation (9)].

Another important issue is the occurrence of antiphase domains. As mentioned above (in §4) the distribution of the diffracted intensity (in the direction parallel to the sample surface) reveals different lateral sizes of the mosaic blocks (or lateral 'coherent lengths') for the odd and even reflections. To explain these observations, we employ the following 'antiphase domain approach': case 1 serves to explain a peak broadening in the $q_{\|}$ direction; case 2 explores the possibility of a peak broadening in the $q_{\perp}$ direction.

A1.1. Case 1. The position of the antiphase domain is obtained by shifting two regions of the lattice relative to each other along the [0001] direction by an amount of relative length Z = 1/2. The wall between the two domains may be thought to be perpendicular to the [11.0] direction, thus leading to a reduction of the domain size parallel to the sample surface. The structure factor in the shifted block is then given by

$$\begin{aligned}\tilde{F}_{hkl} = {} & \left(r_1 f_{\rm Ga} + w_1 f_{\rm Al}\right) \exp\left[-2\pi i\left(\tfrac{1}{3}h + \tfrac{2}{3}k + Zl\right)\right] \\ & + \left(r_2 f_{\rm Al} + w_2 f_{\rm Ga}\right) \exp\left\{-2\pi i\left[\tfrac{2}{3}h + \tfrac{1}{3}k + \left(\tfrac{1}{2} + Z\right)l\right]\right\} \\ & + f_{\rm N} \exp\left\{-2\pi i\left[\tfrac{1}{3}h + \tfrac{2}{3}k + \left(\tfrac{3}{8} + Z\right)l\right]\right\} \\ & + f_{\rm N} \exp\left\{-2\pi i\left[\tfrac{2}{3}h + \tfrac{1}{3}k + \left(\tfrac{7}{8} + Z\right)l\right]\right\} \\ = {} & F_{hkl} \exp(-2\pi i Z l). \end{aligned} \qquad (14)$$

This results in a phase shift between the domains, *i.e.* $\tilde{F}_{hkl} = -F_{hkl}$, when the Miller index l equals 1, 3 or 5, and thus leads to an additional broadening of the superstructure reflections. In the case that the Miller index l equals 2, 4 or 6, the structure factors are equal ($\tilde{F}_{hkl} = F_{hkl}$). There is thus no phase shift and no additional broadening of the fundamental reflections when this kind of antiphase domain structure is present.

A1.2. Case 2. The position of the antiphase domain is obtained by shifting two regions of the lattice relative to each other along the [11.0] direction by an amount of relative length X. The wall between the two domains may be thought to be perpendicular to the [0001] direction, thus leading to a reduction of the domain size perpendicular to the sample surface. The structure factor in the shifted block is then given by

$$\hat{F}_{hkl} = F_{hkl} \exp[-2\pi i X(h + k)]. \qquad (15)$$

For reflections of type 00l (l = 1 . . . 6) the structure factors are equal:

$$\hat{F}_{hkl} = F_{hkl} \qquad (\textit{i.e.}\ \text{no phase shift}).$$

This means that antiphase domains can produce an additional phase shift between the blocks only with hkl reflections. With

symmetrical reflections $00l$, there is no phase shift and thus no broadening of reflections arising from the presence of this kind of antiphase domain structure.

We would like to thank P. Koidl and K. Köhler (IAF Freiburg), K. W. Benz and D. Ebling (FMF, University Freiburg) for valuable discussions. The Bundesministerium für Bildung Wissenschaft, Forschung und Technologie (BMBF) is thanked for financial support. This work was partly performed at the Australian National Beamline Facility with support from the Australian Synchrotron Research Program, which is funded by the Commonwealth of Australia under the Major National Research Facilities Program. SM acknowledges the support of an Australian Postgraduate Award.

References

Afanas'ev, A. M. & Kohn, V. G. (1971). *Acta Cryst.* A**27**, 421–430.
Albrecht, M., Lymperakis, L., Neugebauer, J., Northrup, J. E., Kirste, L., Leroux, M., Grezegory, I., Porowski, S. & Strunk, H. (2004). In preparation.
Balzar, D. (1999). *Defect and Microstructure Analysis by Diffraction*, edited by R. L. Snyder, J. Fiala & H. J. Bunge, pp. 94–126. Oxford University Press.
Becker, P. & Al Haddad, M. (1990). *Acta Cryst.* A**46**, 123–129.
Becker, P. & Al Haddad, M. (1992). *Acta Cryst.* A**48**, 121–134.
Bellon, P., Chevalier, J. P., Augarde, E., Andre, J. P. & Martin, G. P. (1989). *J. Appl. Phys.* **66**, 2388–2394.
Benamara, M., Kirste, L., Albrecht, M., Benz, K. W. & Strunk, H. (2003). *Appl. Phys. Lett.* **82**, 547–549.
Bushuev, V. A. (1989*a*). *Sov. Phys. Solid State*, **31**, 1877–1882.
Bushuev, V. A. (1989*b*). *Sov. Phys. Crystallogr.* **34**, 163–167.
Dudiy, S. V. & Zunger, A. (2003). *Phys. Rev. B*, **68**, 041302R.
Follstaedt, D. M., Schneider, R. P. Jr & Jones, E. D. (1994). *J. Appl. Phys.* **77**, 3077–3087.
Guigay, J. P. & Chukhovskii, F. N. (1995). *Acta Cryst.* A**51**, 288–294.
Halder, N. C. & Wagner, C. N. J. (1966). *Acta Cryst.* **20**, 312–313.
Herres, N., Fuchs, F., Schmitz, J., Pavlov, K. M., Wagner, J., Ralston, J. D., Koidl, P., Gadaleta, C. & Scamarcio, G. (1996). *Phys. Rev. B*, **53**, 15688–15705.
Herres, N., Kirste, L., Obloh, H., Köhler, K., Wagner, J. & Koidl, P. (2002). *Mater. Sci. Eng. B*, **91–92**, 425–432.
Herres, N., Obloh, H., Bachem, K. H. & Helming, K. (1999). *Mater. Sci. Eng. B*, **59**, 202–206.
Heying, B., Wu, X. H., Keller, S., Li, Y., Kapolnek, D., Keller, B. P., DenBaars, S. P. & Speck, J. S. (1996) *Appl. Phys. Lett.* **68**, 643–645.
Holý, V., Wolf, K., Kastner, M., Stanzl, H. & Gebhardt, W. J. (1994). *J. Appl. Cryst.* **27**, 551–557.
Iida, A. & Kohra, K. (1979) *Phys. Status Solidi A*, **51**, 533–542.
Iliopoulos, E., Ludwig, K. F. Jr, Moustakas, T. D., Komniou, Ph., Karakostas, Th., Nouet, G. & Chu, S. N. G. (2001). *Mater. Sci. Eng. B*, **87**, 227–236.
Kaganer, V. M., Köhler, R., Schmidbauer, M., Opitz, R. & Jenichen, B. (1997). *Phys. Rev. B*, **55**, 1793–1810.
Kato, N. (1980). *Acta Cryst.* A**36**, 763–769, 770–778.
Kato, N. (1982). *Z. Naturforsch. Teil A*, **87**, 485–489.
Kato, N. (1991). *Acta Cryst.* A**47**, 1–11.
Kato, N. (1994). *Acta Cryst.* A**50**, 17–22.
Korakakis, D., Ludwig, K. F. Jr & Moustakas, T. D. (1997). *Appl. Phys. Lett.* **71**, 72–74.
Krivoglaz, M. A. (1996). *X-ray and Neutron Diffraction in Nonideal Crystals*. Berlin: Springer.
Laügt, M., Bellet-Amalric, E., Ruterana, P. & Omnès, F. (2003). *Phys. Status Solidi B*, **236**, 729–739.
Nesterets, Y. I. & Punegov, V. I. (2000). *Acta Cryst.* A**56**, 540–548.
Pavlov, K. M. & Punegov, V. I. (1998). *Acta Cryst.* A**54**, 214–218.
Pavlov, K. M. & Punegov, V. I. (2000). *Acta Cryst.* A**56**, 227–234.
Pavlov, K. M. & Punegov, V. I. (2005). In preparation.
Ratnikov, V. V., Kyutt, R. N., Shubina, T. V., Paskova, T. & Monemar, B. (2001). *J. Phys. D Appl. Phys.* **10A**, A30–A34.
Schneider, J. R., Bouchard, R., Graf, H. A. & Nagasawa, H. (1992). *Acta Cryst.* A**48**, 804–819.
Takagi, S. (1969). *J. Phys. Soc. Jpn*, **26**, 1239–1253.
Takama, T. & Harima, H. (1994). *Acta Cryst.* A**50**, 239–246.
Warren, B. E. (1969). *X-ray Diffraction*. Reading, Mass.: Addison-Wesley.
Williamson, G. K. & Hall, G. K. (1953). *Acta Metall.* **1**, 22–31.
Wright, A. F., Leung, K. & van Schilfgaarde, M. (2001). *Appl. Phys. Lett.* **78**, 189–191.
Zunger, A. & Marhajan, S. (1994). *Handbook on Semiconductors*, Vol. 3, edited by T. S. Moss, pp. 1399–1514. Amsterdam: Elsevier.